WILEY-VCH

Edited by Hugo E. Hernández-Figueroa,
Erasmo Recami, and Michel Zamboni-Rached

Non-Diffracting Waves

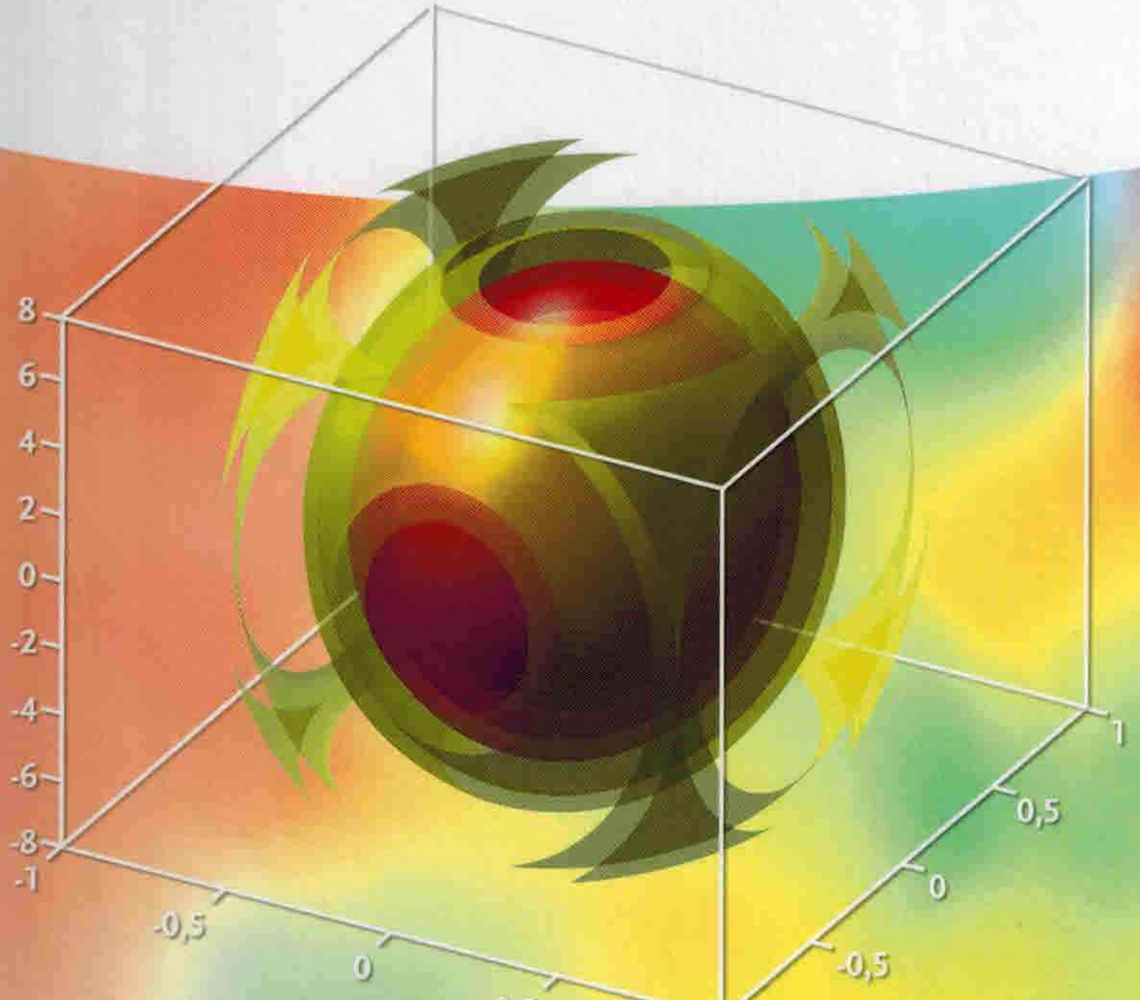

Related Titles

Couairon, A., Mysyrowicz, A.

Nonlinear propagation of ultrashort laser pulses

From fundamentals to filamentation and self-focusing

2015
Print ISBN: 978-3-527-41186-3

Hernández-Figueroa, H.E., Zamboni-Rached, M., Recami, E. (eds.)

Localized Waves

2008
Print ISBN: 978-0-470-10885-7

Contents

5

Limited-Diffraction Beams for High-Frame-Rate Imaging

Jian-yu Lu

5.1

Introduction

In the first volume of this book [1], the author reviewed Bessel beams [2, 3], X waves [4–8], other limited-diffraction beams [9–15], and their various applications such as high-frame-rate (HFR) imaging [16–18], extended HFR imaging [19–30], fast computation of wave fields [31], biomedical tissue characterization [32], pulse-echo medical imaging [33–35], blood flow velocity vector imaging [36, 37], nondestructive evaluation of materials (NDE) [38], optical coherent tomography (OCT) [39], high-speed optical communications [40, 41], and high-resolution two-way dynamic focusing imaging [42]. In addition, limited-diffraction solutions to the Klein–Gordon equation and Schrödinger equation, as well as these solutions in confined spaces were obtained [1]. For readers who are interested in getting more information, 190 references have been provided in [1] including some review papers on X waves and their applications [43–45]. Bessel beams, X waves, and related localized waves have also been studied extensively by many other investigators [46–61]. Due to their potential applications in various fields, X waves were featured in the magazine *Physics Today* [8].

The terminology "limited-diffraction beams" is a general term representing all beams or waves that are propagation invariant, that is, in theory, the shapes of these beams remain the same as they propagate to an infinite distance [62]. Among limited-diffraction beams, those that have a localized center, such as Bessel beams [2, 3] and X waves [4–8], are of particular interest.

Based on the theory of limited-diffraction beams such as the Bessel beams and X waves, a HFR two-dimensional (2D) and three-dimensional (3D) imaging method was developed [16–18] and extended [19–30]. To understand this method, it is helpful to explain how conventional imaging methods work. In the conventional imaging methods such as delay-and-sum (D&S) [63] and pulse-echo radar imaging [64], a broadband beam focused in one direction is transmitted to illuminate objects such as biological soft tissues with a planer array transducer (a transducer consisting of multiple elements arranged either along a line or on a rectangular grid with an equal distance between elements) [65]. Because individual cells in the biological

Non-Diffracting Waves, First Edition.
Edited by Hugo E. Hernández-Figueroa, Erasmo Recami, and Michel Zamboni-Rached.

soft tissues can scatter incoming waves in all directions, part of the waves are scattered back to the array transducer that transmits the waves. The scattered waves are then converted to electrical signals (received signals) representing the backscattered waves by the array transducer. The received signals (echo signals) are not only a function of time, but also a function of the position of the element of the array transducer. With the received signals, a line of images is reconstructed by properly delaying the signals from each element and then summing the delayed signals to produce a focused receive beam whose focus tracks echoes dynamically along the direction of the transmit beam as the echoes return from a deeper and deeper depth with time. After getting a line of image, a new beam is transmitted in a slightly different direction than the previous one and then the received echo signals corresponding to this beam are used to reconstruct another line of image. This process is repeated until an entire image, which usually covers a 90° field of view, is reconstructed.

Due to the line-by-line imaging process and the fact that each beam takes time to propagate from the surface of the transducer to a certain depth of interest and then return, it needs quite a long time to reconstruct an image in the case of ultrasound. For example, assuming that we would like to get an image that has a sector shape with its apex on the center of the surface of the transducer, where the sector consists of 91 lines, the image depth (or sector radius) is 240 mm, and the ultrasound speed of sound is about $1.5\,\mathrm{mm}\,\mu\mathrm{s}^{-1}$ in biological soft tissues, it will take $((240 \times 2) \times 91)/1.5 = 29\,120\,\mu\mathrm{s}$ to reconstruct an image. This limits the maximum image frame rate to about 34 FPS. Since the human heart completes a beat in about one second, this frame rate is inadequate to extract parameters of moving structures such as the mitral valve and blood flow for medical diagnoses. If a 3D image is reconstructed from a 3D object, the image frame rate will be further reduced by another 91, that is, $34/91 = 0.37$ FPS, assuming 91 slices are used to form a frame of the 3D image.

To increase the image frame rate, it is important to develop an imaging method that is not based on the line-by-line principle. The HFR imaging method is such a method that allows reconstructing one image from each transmit beam [16–18]. A proposed system of the HFR imaging method is shown in Figure 5.1 [21], where broad beams (as opposed to the narrowly focused beam in the D&S method above) such as steered plane waves or limited-diffraction array beams are used in transmission to illuminate the entire object [19–23] (also see claims 8 and 9 for steered plane waves and claim 3 for limited-diffraction beams in [18]). Then, limited-diffraction array beams or simply spatial Fourier transforms are used to reconstruct images. To simplify the imaging system, the steps that convert echo signals to optical and then recover them from the optical signals can be eliminated by integrating the image reconstruction electronics into an ultrasound probe that doctors hold to scan patients and acquire data. After images are reconstructed, they are transmitted wirelessly to an external display unit (see claims in [21]). The frame rate of the HFR imaging approach can be calculated using the example above. Since the entire object is illuminated by one broad transmit beam to reconstruct a 3D image, the time needed to reconstruct a frame of image is only about $(240 \times 2)/1.5 = 320\,\mu\mathrm{s}$. This translates to an ultra-high image frame rate of about

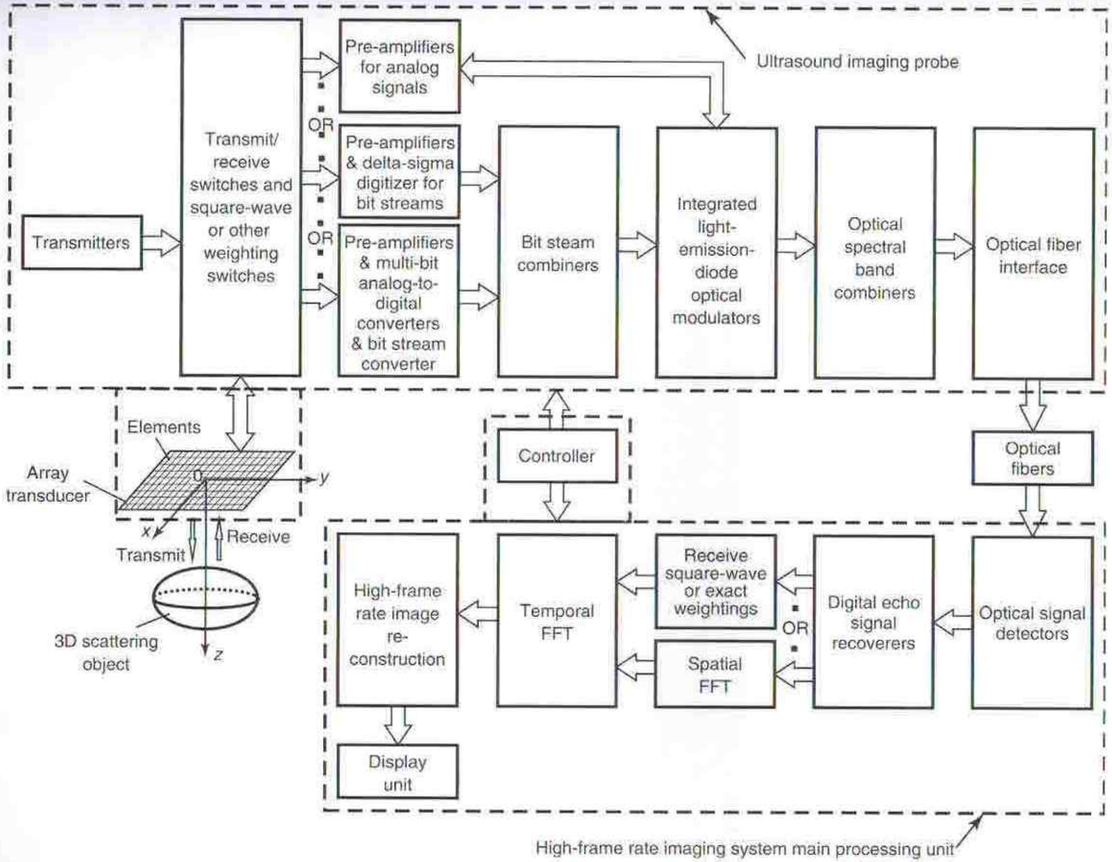

Figure 5.1 An example of a high-frame-rate (HFR) imaging system (modified from [21]). The entire system can also be integrated into the probe box above and the reconstructed images can be transmitted wirelessly as described in the claims in [21].

3125 FPS for either 2D or 3D imaging. This is useful for functional ultrasound imaging, elasticity imaging, blood flow velocity vector imaging, and strain and strain rate imaging of fast moving objects such as the heart [28, 29, 36, 37, 66, 67]. Because of its importance, the HFR imaging method was regarded as one of the predictions of the twenty-first century medical ultrasound in 2000 [68].

In this chapter, the theory of the HFR imaging method [16–23] and its relationship with limited-diffraction beams such as the Bessel beams [2, 3] and X waves [4–8] will be reviewed. Various improvements, developments, and applications of the HFR imaging method will be presented [9–15, 24–45, 62, 65, 76–77, 82, 86–88].

5.2
Theory of Limited-Diffraction Beams

5.2.1
Generalized Solutions to Wave Equation

An N-dimensional isotropic/homogeneous wave equation is given by

$$\left[\sum_{j=1}^{N} \frac{\partial^2}{\partial x_j^2} - \frac{1}{c^2}\frac{\partial^2}{\partial t^2}\right]\Phi(\mathbf{r}, t) = 0 \tag{5.1}$$

where x_j $(j = 1, 2, \ldots, N)$ represents rectangular coordinates in an N-dimensional space, $N \geq 1$ is an integer, $\Phi(\mathbf{r}, t)$ is a scalar function (sound pressure, velocity potential, or Hertz potential in electromagnetics) of spatial variables, $\mathbf{r} = (x_1, x_2, \ldots, x_N)$, and time, t. c is the speed of sound in a medium (or the speed of light in vacuum) [19, 44].

In 3D space, we have:

$$\left(\nabla^2 - \frac{1}{c^2}\frac{\partial^2}{\partial t^2}\right)\Phi(\mathbf{r}, t) = 0 \tag{5.2}$$

where ∇^2 is the Laplace operator. In cylindrical coordinates, the wave equation is given by

$$\left[\frac{1}{r}\frac{\partial}{\partial r}\left(r\frac{\partial}{\partial r}\right) + \frac{1}{r^2}\frac{\partial^2}{\partial \phi^2} + \frac{\partial^2}{\partial z^2} - \frac{1}{c^2}\frac{\partial^2}{\partial t^2}\right]\Phi(\mathbf{r}, t) = 0 \tag{5.3}$$

where $r = \sqrt{x^2 + y^2}$ is the radial distance, $\phi = \tan^{-1}(y/x)$ is the polar angle, and z is the axial axis.

One generalized solution to the N-dimensional wave equation in Equation 5.1 is given by [5, 43, 44]

$$\Phi(x_1, x_2, \ldots, x_N; t) = f(s) \tag{5.4}$$

where

$$s = \sum_{j=1}^{N-1} D_j x_j + D_N(x_N \pm c_1 t), \; N \geq 1 \tag{5.5}$$

and where D_j are complex coefficients, $f(s)$ is any well-behaved complex function of s, and

$$c_1 = c\sqrt{1 + \sum_{j=1}^{N-1} D_j^2 / D_N^2} \tag{5.6}$$

If c_1 is real, $f(s)$ and its linear superposition represent limited-diffraction solutions to the N-dimensional wave equation (Equation 5.1).

For example, if $N = 3,\ x_1 = x,\ x_2 = y,\ x_3 = z,\ D_1 = \alpha_0(k,\zeta)\cos\theta,\ D_2 = \alpha_0(k,\zeta)\sin\theta,\ D_3 = b(k,\zeta)$, with cylindrical coordinates, one obtains families of solutions to Equation 5.3 [5, 43, 44]:

$$\Phi_\zeta(s) = \int_0^\infty T(k)\left[\frac{1}{2\pi}\int_{-\pi}^{\pi} A(\theta) f(s) \mathrm{d}\theta\right]\mathrm{d}k \tag{5.7}$$

and

$$\Phi_K(s) = \int_{-\pi}^{\pi} D(\zeta)\left[\frac{1}{2\pi}\int_{-\pi}^{\pi} A(\theta) f(s) \mathrm{d}\theta\right]\mathrm{d}\zeta \tag{5.8}$$

where

$$s = \alpha_0(k,\zeta) r\cos(\phi - \theta) + b(k,\zeta)[z \pm c_1(k,\zeta)t] \tag{5.9}$$

and where

$$c_1(k,\zeta) = c\sqrt{1 + [\alpha_0(k,\zeta)/b(k,\zeta)]^2} \tag{5.10}$$

and $\alpha_0(k,\zeta)$, $b(k,\zeta)$, $A(\theta)$, $T(k)$, and $D(\zeta)$ are well-behaved functions, and θ, k, and ζ are free parameters. If $c_1(k,\zeta)$ is real, and is not a function of k and ζ respectively, $\Phi_\zeta(s)$ and $\Phi_K(s)$ are families of limited-diffraction solutions to the wave equation (Equation 5.3).

The following function is also a family of limited-diffraction solution to the wave equation [5, 43, 44], which represents waves that can propagate to an infinite distance without changing their wave shape at the speed of c:

$$\Phi_L(r,\phi,z-ct) = \Phi_1(r,\phi)\Phi_2(z-ct) \tag{5.11}$$

where $\Phi_2(z-ct)$ is any well-behaved function of $z - ct$ and $\Phi_1(r,\phi)$ is a solution to the transverse Laplace equation:

$$\left[\frac{1}{r}\frac{\partial}{\partial r}\left(r\frac{\partial}{\partial r}\right) + \frac{1}{r^2}\frac{\partial^2}{\partial\phi^2}\right]\Phi_1(r,\phi) = 0 \tag{5.12}$$

5.2.2
Bessel Beams and X Waves

5.2.2.1 Bessel Beams

If $T(k) = \delta(k - k')$, $f(s) = \mathrm{e}^s$, $\alpha_0(k, \zeta) = -i\alpha$, and $b(k, \zeta) = i\beta$ in Equation 5.7 and Equation 5.9, we have:

$$\Phi_\zeta(s) = \left[\frac{1}{2\pi}\int_{-\pi}^{\pi} A(\theta)\mathrm{e}^{-i\alpha r\cos(\phi-\theta)}\mathrm{d}\theta\right]\mathrm{e}^{i(\beta z-\omega t)} \tag{5.13}$$

where $\beta = \sqrt{k'^2 - \alpha^2}$ is the propagation parameter, $\delta(k - k')$ is the Dirac-Delta function, and $k' = \omega/c > 0$ is the wave number and ω is the angular frequency. If $A(\theta) = i^n\mathrm{e}^{in\theta}$, one obtains an nth-order Bessel beam [2, 3, 26, 27]:

$$\Phi_{B_n}(\mathbf{r}, t) = \Phi_{B_n}(r, \phi, z - c_1 t) = \mathrm{e}^{in\phi}J_n(\alpha r)\mathrm{e}^{i(\beta z-\omega t)}, n = 0, 1, 2, \ldots \tag{5.14}$$

where the subscript "B_n" means an nth-order Bessel beam, α is a scaling parameter, $J_n(\cdot)$ is the nth-order Bessel function of the first kind, and $c_1 = \omega/\beta$ is the phase velocity of the wave. It is clear that Bessel beams are single-frequency waves and are localized in transverse direction. The scaling parameter, α, determines the degree of localization.

5.2.2.2 X Waves

If $T(k) = B(k)\mathrm{e}^{-a_0 k}$, $A(\theta) = i^n\mathrm{e}^{in\theta}$, $\alpha_0(k, \zeta) = -ik\sin\zeta$, $b(k, \zeta) = ik\cos\zeta$, and $f(s) = \mathrm{e}^s$ in Equation 5.7 and Equation 5.9, one obtains an nth-order X wave [4–8], which is a superposition of limited-diffraction portion of Axicon beams [49]:

$$\begin{aligned}\Phi_{X_n}(\mathbf{r}, t) &= \Phi_{X_n}(r, \phi, z - c_1 t)\\ &= \mathrm{e}^{in\phi}\int_0^\infty B(k)J_n(kr\sin\zeta)\mathrm{e}^{-k[a_0 - i\cos\zeta(z-c_1 t)]}\mathrm{d}k, \quad n = 0, 1, 2, \ldots\end{aligned} \tag{5.15}$$

where the subscript "X_n" means an nth-order X wave, $c_1 = c/\cos\zeta \geq c$ is both the phase and group velocity of the wave, $|\zeta| < \pi/2$ is the Axicon angle [49] of X waves, a_0 is a positive free parameter that determines the decaying speed of the high-frequency components of the wave, and $B(k)$ is an arbitrary well-behaved transfer function of a device (acoustic transducer or electromagnetic antenna) that produces the wave.

Compare Equation 5.15 with Equation 5.14. It is easy to see the similarity and difference between a Bessel beam and an X wave. X waves are multiple-frequency waves while Bessel beams have a single frequency. However, both waves have the same limited-diffraction property, that is, they are propagation invariant. Because of multiple frequencies, X waves can be localized in both transverse space and time to form a tight wave packet. They can propagate in the free space or isotropic/homogeneous media without spreading or dispersion.

Choosing specific $B(k)$, one can obtain analytical X wave solutions [4–8] from Equation 5.15. One example is the zeroth-order X wave where $n = 0$ and $B(k) = a_0$ [5]:

$$\begin{aligned}\Phi_{X_0}(\mathbf{r},t) = \Phi_{X_0}(r,\phi,z-c_1t) &= \int_0^{\infty} a_0 J_0(kr\sin\zeta)\mathrm{e}^{-k[a_0-i\cos\zeta(z-c_1t)]}\mathrm{d}k \\ &= \frac{a_0}{\sqrt{(r\sin\zeta)^2+[a_0-i\cos\zeta(z-c_1t)]^2}}\end{aligned} \tag{5.16}$$

5.2.3
Limited-Diffraction Array Beams

Renaming $\mathbf{r}=(x,y,z)$ with $\mathbf{r}_0=(x_0,y_0,z_0)$, (r,ϕ,z) with (r_0,ϕ_0,z_0), ζ with ζ_T, and θ with θ_T in the rest of the chapter, and then summing the X waves in Equation 5.15 over the index, n, with the weight, $i^n\mathrm{e}^{-in\theta_T}$, broadband limited-diffraction array beams [12, 37] or pulsed steered plane waves (a plane wave is a special case of limited-diffraction beams) are obtained, which are also limited-diffraction solutions to Equation 5.1 (see Equation 3 of [16]) [19]:

$$\begin{aligned}\Phi^{\mathrm{T}}_{\mathrm{array}}(\mathbf{r}_0,t) &= \sum_{n=-\infty}^{\infty} i^n\mathrm{e}^{-in\theta_\mathrm{T}}\Phi_{X_n}(r_0,\phi_0,z_0-c_1t) \\ &= \int_0^{\infty} B(k)\left[\sum_{n=-\infty}^{\infty} i^n J_n\left(kr_0\sin\zeta_\mathrm{T}\right)\mathrm{e}^{in(\phi_0-\theta_\mathrm{T})}\right] \\ &\quad\times \mathrm{e}^{-k[a_0-i\cos\zeta_T(z_0-c_1t)]}\mathrm{d}k\end{aligned} \tag{5.17}$$

where $0\le\theta_\mathrm{T}<2\pi$ is a free parameter representing an azimuthal angle, the superscript "T" in $\Phi^{\mathrm{T}}_{\mathrm{array}}(\mathbf{r}_0,t)$ means "transmission," and the subscript "array" represents "array beams." Because of the following equality [69],

$$\sum_{n=-\infty}^{\infty} i^n J_n(kr_0\sin\zeta_\mathrm{T})\mathrm{e}^{in(\phi_0-\theta_\mathrm{T})} = \mathrm{e}^{i(kr_0\sin\zeta_\mathrm{T})\cos(\phi_0-\theta_\mathrm{T})} \tag{5.18}$$

and the relationship,

$$\begin{cases} k_{x_\mathrm{T}} = k\sin\zeta_\mathrm{T}\cos\theta_\mathrm{T} = k_{1_\mathrm{T}}\cos\theta_\mathrm{T} \\ k_{y_\mathrm{T}} = k\sin\zeta_\mathrm{T}\sin\theta_\mathrm{T} = k_{1_\mathrm{T}}\sin\theta_\mathrm{T} \\ k_{z_\mathrm{T}} = k\cos\zeta_\mathrm{T} = \sqrt{k^2-k_{1_\mathrm{T}}^2}\ge 0, \text{where } k_{1_\mathrm{T}} = \sqrt{k_{x_\mathrm{T}}^2+k_{y_\mathrm{T}}^2} = k\sin\zeta_\mathrm{T}\end{cases} \tag{5.19}$$

where k_{x_T} and k_{y_T} are projections of the transmission wave vector along the x_1 and y_1 axes (in the rest of the chapter we assume that $\mathbf{r}_1=(x_1,y_1,0)$ is a point at the surface of a planar transducer [65]), respectively, the array beams can be written as the following Fourier transform pair in terms of time, (see Equations 5 and 6 of [16]):

$$\begin{cases} \Phi^{\mathrm{T}}_{\mathrm{array}}\left(\mathbf{r}_0,t\right) = \frac{1}{2\pi}\int_{-\infty}^{\infty} A(k)H(k)\mathrm{e}^{ik_{x_\mathrm{T}}x_0+ik_{y_\mathrm{T}}y_0+ik_{z_\mathrm{T}}z_0}\mathrm{e}^{-i\omega t}\mathrm{d}k \\ \widetilde{\Phi}^{\mathrm{T}}_{\mathrm{array}}(\mathbf{r}_0,\omega) = \frac{A(k)H(k)}{c}\mathrm{e}^{ik_{x_\mathrm{T}}x_0+ik_{y_\mathrm{T}}y_0+ik_{z_\mathrm{T}}z_0}\end{cases} \tag{5.20}$$

where $A(k) = 2\pi B(k)\mathrm{e}^{-ka_0}$ is a transmitting transfer function of the transducer elements that includes both the electrical response of the driving circuits and the electro-acoustical coupling characteristics [70] and $H(\omega/c) = \{1, \omega \geq 0; 0, \omega < 0\}$ is the Heaviside step function [71]. The spectrum of the array beam in Equation 5.20 is an expression of a monochromatic (single angular frequency ω) plane wave steered at the direction along the transmission wave vector, $\mathbf{K}^{\mathrm{T}} = (k_{x_{\mathrm{T}}}, k_{y_{\mathrm{T}}}, k_{z_{\mathrm{T}}})$.

Similar to Equation 5.20, the response of the transducer [65] weighted with a broadband limited-diffraction array beam [12, 37] or pulsed steered plane wave for a point source (or scatterer) located at $\mathbf{r}_0$ is given by the following Fourier transform pair due to the reciprocal principle:

$$\begin{cases} \Phi^{\mathrm{R}}_{\mathrm{array}}(\mathbf{r}_0, t) = \frac{1}{2\pi}\displaystyle\int_{-\infty}^{\infty} T(k)H(k)\mathrm{e}^{ik_x x_0 + ik_y y_0 + ik_z z_0}\mathrm{e}^{-i\omega t}\mathrm{d}k \\ \widetilde{\Phi}^{\mathrm{R}}_{\mathrm{array}}(\mathbf{r}_0, \omega) = \frac{T(k)H(k)}{c}\mathrm{e}^{ik_x x_0 + ik_y y_0 + ik_z z_0} \end{cases} \tag{5.21}$$

where the superscript "R" means "reception," $T(k)$ is the transfer function of the transducer in reception, $\widetilde{\Phi}^{\mathrm{R}}_{\mathrm{array}}(\mathbf{r}_0, \omega)$ is an expression of a monochromatic plane wave response steered at the direction along the reception wave vector, $\mathbf{K}^{\mathrm{R}} = (k_x, k_y, k_z)$, where k_x and k_y are projections of the reception wave vector along the x_1 and y_1 axes, respectively, and $k_z = \sqrt{k^2 - k_x^2 - k_y^2} \geq 0$.

5.3
Received Signals

5.3.1
Pulse-Echo Signals and Relationship with Imaging

If the same array transducer is used as both a transmitter and a receiver, from Equation 5.20 and Equation 5.21, the received signal for the wave scattered from all point scatterers inside the volume, V, of an object function, $f(\mathbf{r}_0)$ (representing the scattering strength of a scatterer at point $\mathbf{r}_0$), is given by a linear superposition of individual scattering sources over V. This signal can be represented by the following Fourier transform pair in terms of time (see Equations 13 and 15 of [16]) [19]:

$$\begin{cases} R_{k_x+k_{x_{\mathrm{T}}}, k_y+k_{y_{\mathrm{T}}}, k_z+k_{z_{\mathrm{T}}}}(t) = \displaystyle\int_V f(\mathbf{r}_0)[\Phi^{\mathrm{T}}_{\mathrm{array}}(\mathbf{r}_0, t) * \Phi^{\mathrm{R}}_{\mathrm{array}}(\mathbf{r}_0, t)]\mathrm{d}\mathbf{r}_0 \\ = \frac{1}{2\pi}\displaystyle\int_{-\infty}^{\infty} \frac{A(k)T(k)H(k)}{c}\left[\int_V f(\mathbf{r}_0)\,\mathrm{e}^{i(k_x+k_{x_{\mathrm{T}}})x_0 + i(k_y+k_{y_{\mathrm{T}}})y_0 + i(k_z+k_{z_{\mathrm{T}}})z_0}\mathrm{d}\mathbf{r}_0\right]\mathrm{e}^{-i\omega t}\mathrm{d}k \\ = \frac{1}{2\pi}\displaystyle\int_{-\infty}^{\infty} \frac{A(k)T(k)H(k)}{c}F(k_x + k_{x_{\mathrm{T}}}, k_y + k_{y_{\mathrm{T}}}, k_z + k_{z_{\mathrm{T}}})\mathrm{e}^{-i\omega t}\mathrm{d}k \\ \widetilde{R}_{k'_x, k'_y, k'_z}(\omega) = \frac{A(k)T(k)H(k)}{c^2}F(k'_x, k'_y, k'_z) \end{cases} \tag{5.22}$$

where

$$\begin{cases} k'_x = k_x + k_{x_T} \\ k'_y = k_y + k_{y_T} \\ k'_z = k_z + k_{z_T} = \sqrt{k^2 - k_x^2 - k_y^2} + \sqrt{k^2 - k_{x_T}^2 - k_{y_T}^2} \geq 0 \end{cases} \tag{5.23}$$

and "*" represents the convolution with respect to time t. This is due to the fact that the spectrum of the convolution of two functions is equal to the product of the spectra of the functions, and an assumption that the imaging system is linear and multiple scattering can be ignored (first born or weak scattering approximation [72, 73]). The 3D spatial Fourier transform in Equation 5.22 is defined the same as that in Equation 14 of [16]. The relationship between the one-dimensional (1D) temporal Fourier transform (spectrum) of the received echo signal that is weighted by a limited-diffraction array beam [12, 37] and the 3D spatial Fourier transform of the object function is the key for image reconstructions (see Equations 16, 18, and 22 of [16]).

5.3.2
Limited-Diffraction Array Beam Aperture Weighting and Spatial Fourier Transform of Echo Signals

Using Equation 5.20 and Equation 5.21, it is clear that Equation 5.22 can be rewritten as follows:

$$\begin{aligned} \widetilde{R}_{k'_x,k'_y,k'_z}(\omega) &= \int_V f(\mathbf{r}_0)\widetilde{\Phi}^{\mathrm{T}}_{\mathrm{array}}(\mathbf{r}_0,\omega)\widetilde{\Phi}^{\mathrm{R}}_{\mathrm{array}}(\mathbf{r}_0,\omega)\mathrm{d}\mathbf{r}_0 \\ &= \int_V f(\mathbf{r}_0)\widetilde{\Phi}^{\mathrm{T}}_{\mathrm{array}}(\mathbf{r}_0,\omega)\Im_{x_1,y_1}\{\Im^{-1}_{k_x,k_y}[\widetilde{\Phi}^{\mathrm{R}}_{\mathrm{array}}(\mathbf{r}_0,\omega)]\}\mathrm{d}\mathbf{r}_0 \\ &= \Im_{x_1,y_1}\left\{\int_V \left[f\left(\mathbf{r}_0\right)\widetilde{\Phi}^{\mathrm{T}}_{\mathrm{array}}(\mathbf{r}_0,\omega)\right]\left[-\frac{T\left(k\right)H(k)}{2\pi c}\frac{\partial}{\partial z_0}\right.\right. \\ &\quad \left.\left.\left(\frac{\mathrm{e}^{ik\sqrt{(x_1-x_0)^2+(y_1-y_0)^2+z_0^2}}}{\sqrt{(x_1-x_0)^2+(y_1-y_0)^2+z_0^2}}\right)\right]\mathrm{d}\mathbf{r}_0\right\} \end{aligned} \tag{5.24}$$

where the last equal sign in Equation 5.24 is due to the shift theorem of Fourier transform and the following equality (see Equation 13 of [74]):

$$\mathrm{e}^{ik_z z_0} = -\frac{1}{2\pi}\Im_{x_1,y_1}\left\{\frac{\partial}{\partial z_0}\left(\frac{\mathrm{e}^{ik\sqrt{{x_1}^2+{y_1}^2+z_0^2}}}{\sqrt{{x_1}^2+{y_1}^2+z_0^2}}\right)\right\} \tag{5.25}$$

where $\Im_{x_1,y_1}$ represents a 2D Fourier transform in terms of both x_1 and y_1 at the transducer surface and $\Im^{-1}_{k_x,k_y}$ is an inverse 2D Fourier transform in terms of both

k_x and k_y. Because the term

$$-\frac{1}{2\pi}\frac{\partial}{\partial z_0}\left(\frac{e^{ik\sqrt{(x_1-x_0)^2+(y_1-y_0)^2+z_0^2}}}{\sqrt{(x_1-x_0)^2+(y_1-y_0)^2+z_0^2}}\right) \tag{5.26}$$

in Equation 5.24 is the kernel of the Rayleigh–Sommerfeld diffraction formula (see Equations 3–36 of [75] and [74]), it represents the field produced at $\mathbf{r}_1 = (x_1, y_1, 0)$ due to a point source (scatterer) located at $\mathbf{r}_0 = (x_0, y_0, z_0)$. It is clear that if the transmission array beam, $\widetilde{\Phi}^{\mathrm{T}}_{\mathrm{array}}(\mathbf{r}_0, \omega)$, is replaced with an arbitrary beam, Equation 5.24 is still valid. The effects of the transmission beam and the object function, $f(\mathbf{r}_0)$, in Equation 5.24 are to modulate the phase and amplitude of secondary point sources at $\mathbf{r}_0$. This proves that the limited-diffraction array beam aperture weightings (represented by $\widetilde{\Phi}^{\mathrm{R}}_{\mathrm{array}}(\mathbf{r}_0, \omega)$) [16–18, 76, 77] of echo signals are identical to the 2D spatial Fourier transform of the signals over the same transducer aperture, $\mathbf{r}_1$, even for an arbitrary transmission beam. Because an arbitrary transmission beam can always be expanded in terms of an array beam [12, 37], in principle, Equation 5.24 or Equation 5.22 can be used to reconstruct images for more complicated transmission schemes [75].

5.3.3
Special Case for 2D Imaging

Equation 5.22 and Equation 5.23 give a general 3D image reconstruction formula that is similar to Equation 15 of [16]. They are readily suitable for 2D image reconstructions. Setting one of the transverse coordinates, for example, $k_y = k_{y_T} = 0$, one obtains a 2D imaging formula (see Equation 34 of [16]) [22]:

$$F_{\mathrm{BL}}(k'_x, k'_z) = c^2 H(k) \widetilde{R}_{k'_x, k'_z}(\omega) \tag{5.27}$$

where

$$\begin{cases} k'_x = k_x + k_{x_T} \\ k'_z = k_z + k_{z_T} = \sqrt{k^2 - k_x^2} + \sqrt{k^2 - k_{x_T}^2} \geq 0 \end{cases} \tag{5.28}$$

and $F_{\mathrm{BL}}(k'_x, k'_y, k'_z) = A(k)T(k)F(k'_x, k'_y, k'_z)$ is a band-limited version of the spatial Fourier transform of the object function, the subscript "BL" means "band-limited" (its 2D version is given by $F_{\mathrm{BL}}(k'_x, k'_z) = A(k)T(k)F(k'_x, k'_z)$). In practice, it is the band-limited version of an object function that is reconstructed because of the bandwidth limitation in any practical systems.

5.4
Imaging with Limited-Diffraction Beams

The relationship between the Fourier transform of an object function and that of received echo signals (Equation 5.22 and Equation 5.23) is very general and flexible in terms of image reconstructions (including both HFR and non-HFR methods). They include many methods developed previously [19]. For example, (i) HFR imaging (plane wave transmission without steering, that is, $k_{x_T} = k_{y_T} = 0$ in Equation 5.23) [16–18]; (ii) steered plane waves (fixing ζ_T and θ_T in Equation 5.19 and Equation 5.23 in each transmission but varying k_x and k_y in image reconstructions, that is, $k_{x_T} = k \sin \zeta_T \cos \theta_T$ and $k_{y_T} = k \sin \zeta_T \sin \theta_T$) [19, 22]; (iii) limited-diffraction array beam imaging, where k_{x_T} and k_{y_T} in Equation 5.23 are fixed in each transmission but k_x and k_y are varied in image reconstructions [19, 22]; (iv) two-way dynamic focusing (both $k_x = k_{x_T}$ and $k_y = k_{y_T}$ in Equation 5.23 for multiple limited-diffraction array beam transmissions and receptions) [16, 42]; and (v) multiple steered plane waves with the same steering angles in each plane-wave transmission and reception ($k_x = k_{x_T} = k \sin \zeta_T \cos \theta_T$ and $k_y = k_{y_T} = k \sin \zeta_T \sin \theta_T$ in Equation 5.23, where ζ_T and θ_T are fixed in each transmission, and are the Axicon angle and the azimuthal angle of X waves, respectively) [78]. These special cases are discussed in detail below:

5.4.1
High-Frame-Rate Imaging Methods

5.4.1.1 Plane-Wave HFR Imaging without Steering

For a plane wave transmission without steering, one has $k_{x_T} = 0$ and $k_{y_T} = 0$. From Equation 5.22 and Equation 5.23, one obtains [22]:

$$F_{\mathrm{BL}}(k_x, k_y, k'_z) = c^2 H(k) \widetilde{R}_{k_x, k_y, k'_z}(\omega) \tag{5.29}$$

where

$$\begin{cases} k'_x = k_x \\ k'_y = k_y \\ k'_z = k + k_z = k + \sqrt{k^2 - k_x^2 - k_y^2} \geq 0 \end{cases} \tag{5.30}$$

which is exactly the same as that of the HFR imaging method (see Equations 8 and 15 of [16]). From Equation 5.29 and Equation 5.30, 3D or 2D images can be reconstructed with Equation 18 of [16].

5.4.1.2 Steered Plane-Wave Imaging

As discussed previously, Equation 5.22 and Equation 5.23 directly give a relationship between the 3D Fourier transform of measured echo signals at the transducer surface and the 3D spatial Fourier transform of the object function for a steered plane wave transmission with fixed Axicon angle (steering angle for plane waves), ζ_T [79], of an X wave [4–8] and the azimuthal angle, θ_T. After getting the spatial Fourier transform of the object function, using Equation 18 of [16], one can reconstruct images with an inverse 3D Fourier transform.

For steered plane waves, one obtains the relationship of the parameters between the Fourier transform of the echoes and the object function (see Equation 5.23 and

Equation 5.28) as follows [22]:

$$\begin{cases} k'_x = k_x + k \sin \zeta_{\mathrm{T}} \cos \theta_{\mathrm{T}} \\ k'_y = k_y + k \sin \zeta_{\mathrm{T}} \sin \theta_{\mathrm{T}} \\ k'_z = k_z + k \cos \zeta_{\mathrm{T}} = \sqrt{k^2 - k_x^2 - k_y^2} + k \cos \zeta_{\mathrm{T}} \geq 0 \end{cases} \tag{5.31}$$

Varying the free parameters, ζ_{T} and θ_{T}, from one transmission to another, one obtains partially overlapped coverage of the spatial Fourier domain. Superposing the resulting partially reconstructed images in space or in their spatial Fourier domain from different transmissions, one obtains the final image. The superposition in the spatial domain can be done either coherently (increasing image resolution and contrast) or incoherently (reducing speckle). In the frequency domain, the superposition can only be done coherently, which in theory, is equivalent to the superposition in the spatial domain. The superposition will also increase the field of view of the final image for transducers of a finite aperture [19, 22, 76, 77].

5.4.1.3 Limited-Diffraction Array Beam Imaging

In this imaging method, the following sets of four limited-diffraction array beams [12, 27] for each pair of $k_{x_{\mathrm{T}}}$ and $k_{y_{\mathrm{T}}}$ are transmitted for 3D imaging (see Equation 5.20) [19–23]:

$$\begin{cases} \Phi^{\mathrm{T}}_{\mathrm{array}(1)}(\mathbf{r}_0, t) = \cos(k_{x_{\mathrm{T}}} x_0) \cos(k_{y_{\mathrm{T}}} y_0) G(z_0, t; k_{x_{\mathrm{T}}}, k_{y_{\mathrm{T}}}) \\ \Phi^{\mathrm{T}}_{\mathrm{array}(2)}(\mathbf{r}_0, t) = \cos(k_{x_{\mathrm{T}}} x_0) \sin(k_{y_{\mathrm{T}}} y_0) G(z_0, t; k_{x_{\mathrm{T}}}, k_{y_{\mathrm{T}}}) \\ \Phi^{\mathrm{T}}_{\mathrm{array}(3)}(\mathbf{r}_0, t) = \sin(k_{x_{\mathrm{T}}} x_0) \cos(k_{y_{\mathrm{T}}} y_0) G(z_0, t; k_{x_{\mathrm{T}}}, k_{y_{\mathrm{T}}}) \\ \Phi^{\mathrm{T}}_{\mathrm{array}(4)}(\mathbf{r}_0, t) = \sin(k_{x_{\mathrm{T}}} x_0) \sin(k_{y_{\mathrm{T}}} y_0) G(z_0, t; k_{x_{\mathrm{T}}}, k_{y_{\mathrm{T}}}) \end{cases} \tag{5.32}$$

where

$$G(z_0, t; k_{x_{\mathrm{T}}}, k_{y_{\mathrm{T}}}) = \frac{1}{2\pi} \int_{-\infty}^{\infty} A(k) H(k) \mathrm{e}^{i k_{z_{\mathrm{T}}} z_0} \mathrm{e}^{-i\omega t} \mathrm{d}k = \Im_{\omega}^{-1} \left\{ \frac{A(k)\, H(k) \mathrm{e}^{i k_{z_{\mathrm{T}}} z_0}}{c} \right\} \tag{5.33}$$

and where $\Im_{\omega}^{-1}$ represents an inverse Fourier transform in terms of ω.

For every set of transmissions, one obtains four areas of coverage in the spatial Fourier domain of $f(\mathbf{r}_0)$, denoted as $\widetilde{R}^{(1)} = \widetilde{R}^{(1)}_{k'_x, k'_y, k'_z}(\omega)$, $\widetilde{R}^{(2)} = \widetilde{R}^{(2)}_{k'_x, k'_y, k'_z}(\omega)$, $\widetilde{R}^{(3)} = \widetilde{R}^{(3)}_{k'_x, k'_y, k'_z}(\omega)$, and $\widetilde{R}^{(4)} = \widetilde{R}^{(4)}_{k'_x, k'_y, k'_z}(\omega)$, respectively, from combinations of the four echo signals (see Equation 5.22):

$$\begin{cases} F_{\mathrm{BL}}(k_x + k_{x_{\mathrm{T}}}, k_y + k_{y_{\mathrm{T}}}, k'_z) = c^2 H(k) \left(\widetilde{R}^{(1)} + i\widetilde{R}^{(2)} + i\widetilde{R}^{(3)} - \widetilde{R}^{(4)}\right) \\ F_{\mathrm{BL}}(k_x + k_{x_{\mathrm{T}}}, k_y - k_{y_{\mathrm{T}}}, k'_z) = c^2 H(k) (\widetilde{R}^{(1)} - i\widetilde{R}^{(2)} + i\widetilde{R}^{(3)} + \widetilde{R}^{(4)}) \\ F_{\mathrm{BL}}(k_x - k_{x_{\mathrm{T}}}, k_y + k_{y_{\mathrm{T}}}, k'_z) = c^2 H(k) (\widetilde{R}^{(1)} + i\widetilde{R}^{(2)} - i\widetilde{R}^{(3)} + \widetilde{R}^{(4)}) \\ F_{\mathrm{BL}}(k_x - k_{x_{\mathrm{T}}}, k_y - k_{y_{\mathrm{T}}}, k'_z) = c^2 H(k) (\widetilde{R}^{(1)} - i\widetilde{R}^{(2)} - i\widetilde{R}^{(3)} - \widetilde{R}^{(4)}) \end{cases} \tag{5.34}$$

From both Equation 5.22 and Equation 5.34, high-quality 3D images that have an equivalent dynamic focusing in both transmission and reception of the traditional D&S method [63, 64] can be reconstructed. Varying the free parameters, $k_{x_{\mathrm{T}}}$ and

k_{y_T}, from one set of transmissions to another, one obtains partially overlapped coverage of the spatial Fourier domain. As in the case of the steered plane wave above, superposing the resulting partially reconstructed images in space or in their spatial Fourier domain from different transmissions, one obtains the final image. The superposition can be done either coherently (increasing image resolution and contrast) or incoherently (reducing speckle). The superposition will also increase the field of view of the final image for transducers of a finite aperture [19, 22, 76, 77].

In the case of 2D imaging, Equation 5.32 and Equation 5.34 can be simplified by setting $k_y = k_{y_T} = 0$ (similar to Equation 34 of [16]):

$$\begin{cases} \Phi^{\mathrm{T}}_{\mathrm{array}(1)}(x_0, z_0, t) = \cos(k_{x_T} x_0) G_1(z_0, t; k_{x_T}) \\ \Phi^{\mathrm{T}}_{\mathrm{array}(2)}(x_0, z_0, t) = \sin(k_{x_T} x_0) G_1(z_0, t; k_{x_T}) \\ F_{\mathrm{BL}}(k_x + k_{x_T}, k'_z) = c^2 H(k)(\widetilde{R}^{(1)}_{k'_x, k'_z}(\omega) + i\widetilde{R}^{(2)}_{k'_x, k'_z}(\omega)) \\ F_{\mathrm{BL}}(k_x - k_{x_T}, k'_z) = c^2 H(k)(\widetilde{R}^{(1)}_{k'_x, k'_z}(\omega) - i\widetilde{R}^{(2)}_{k'_x, k'_z}(\omega)) \end{cases} \tag{5.35}$$

where $G_1(z_0, t; k_{x_T}) = G(z_0, t; k_{x_T}, k_{y_T})$ with $k_{y_T} \equiv 0$.

5.4.2
Other Imaging Methods

5.4.2.1 Two-Way Dynamic Focusing

If both $k_x = k_{x_T}$ and $k_y = k_{y_T}$ are fixed during each transmission, from Equation 5.22 and Equation 5.23, one obtains the two-way dynamic focusing with limited-diffraction beam method developed previously (see Equations 42 and 43, and Figure 13 of [16]) [17, 18, 42]:

$$F_{\mathrm{BL}}(k'_x, k'_y, k'_z) = c^2 H(k) \widetilde{R}_{k'_x, k'_y, k'_z}(\omega) \tag{5.36}$$

where

$$\begin{cases} k'_x = 2k_x \\ k'_y = 2k_y \\ k'_z = 2k_z \geq 0 \end{cases} \tag{5.37}$$

which represents an increased Fourier domain coverage resulting in a higher image resolution. The increased Fourier domain coverage may be equivalent to a dynamic focusing in both transmission and reception in theory. Choosing both k_x and k_y on rectangular grids, one may not need to do any interpolation in the spatial Fourier domain of the object function along these directions. This method also increases the image field of view as compared to the HFR imaging method above [16]. However, because only one line in the Fourier domain is obtained from each transmission, this method may be slow for 3D imaging. In addition, to reconstruct an image of a large field of view, the sampling interval of both k_x and k_y must be small so that they may further increase the number of transmissions needed and thus decrease the image frame rate.

5.4.2.2 Multiple Steered Plane Wave Imaging

Using spherical coordinates in Equation 5.19 or the transmission wave vector, $\mathbf{K}^{\mathrm{T}} = (k_{x_{\mathrm{T}}}, k_{y_{\mathrm{T}}}, k_{z_{\mathrm{T}}})$, one obtains (see Equation 8 and Figure 2 of [16]) [22]:

$$\begin{cases} k_{x_{\mathrm{T}}} = k \sin \zeta_{\mathrm{T}} \cos \theta_{\mathrm{T}} = k_{1_{\mathrm{T}}} \cos \theta_{\mathrm{T}} \\ k_{y_{\mathrm{T}}} = k \sin \zeta_{\mathrm{T}} \sin \theta_{\mathrm{T}} = k_{1_{\mathrm{T}}} \sin \theta_{\mathrm{T}} \\ k_{z_{\mathrm{T}}} = k \cos \zeta_{\mathrm{T}} = \sqrt{k^2 - k_{1_{\mathrm{T}}}^2} \geq 0 \end{cases} \tag{5.38}$$

where ζ_{T} is the Axicon angle [49, 79] of X wave [4–8] or the steering angle of a plane wave, θ_{T} is an angle that determines components of the transmission wave vector in both x_1 and y_1 axes (for a given transmission, both ζ_{T} and θ_{T} are fixed), and

$$k_{1_{\mathrm{T}}} = k \sin \zeta_{\mathrm{T}} = \sqrt{k_{x_{\mathrm{T}}}^2 + k_{y_{\mathrm{T}}}^2} \tag{5.39}$$

is the magnitude of the transverse component of the wave vector in the (x_1, y_1) plane.

Let $k_x \equiv k_{x_{\mathrm{T}}} = k \sin \zeta_{\mathrm{T}} \cos \theta_{\mathrm{T}}$ and $k_y \equiv k_{y_{\mathrm{T}}} = k \sin \zeta_{\mathrm{T}} \sin \theta_{\mathrm{T}}$, the Fourier domain of the object function can be filled up in spherical coordinates, $(2k, \zeta_{\mathrm{T}}, \theta_{\mathrm{T}})$, through multiple transmissions. That is, for each plane wave transmission, an echo signal is received with a plane wave response from the same direction. From Equation 5.22 and Equation 5.23, one obtains Equation 5.36 with the following parameters for 3D imaging:

$$\begin{cases} k'_x = 2k \sin \zeta_{\mathrm{T}} \cos \theta_{\mathrm{T}} \\ k'_y = 2k \sin \zeta_{\mathrm{T}} \sin \theta_{\mathrm{T}} \\ k'_z = k_z + k_{z_{\mathrm{T}}} = 2k \cos \zeta_{\mathrm{T}} \geq 0 \end{cases} \tag{5.40}$$

Soumekh [78] has obtained a similar result from a linear system modeling approach in polar coordinates for 2D imaging. Because the samples in the spatial Fourier domain are very sparse for a larger k (see Equation 5.40), a large number of transmissions at different angles are required to obtain high-frequency components accurately. Compared to the two-way dynamic focusing with limited-diffraction beam approach, more transmissions may be needed to get an adequate coverage of the Fourier space (domain) and thus the image frame rate will be low.

5.5
Mapping between Fourier Domains

To reconstruct images in Equation 5.22 and 5.23 using the fast Fourier transform (FFT) [80], it is necessary to obtain the Fourier transform of the object function at rectangular grids of (k'_x, k'_y, k'_z). However, the Fourier transform of echo data is known only on rectangular grids of (k_x, k_y, k) (notice that digitization of echo signals is in an equal time interval and that an array transducer has an equal distance between adjacent elements [65]), which is related to (k'_x, k'_y, k'_z) by Equation 5.23. In this section, nonlinear mapping of data with Equation 5.23 will be given for two special cases (i.e., the steered plane wave and the limited-diffraction array beam transmissions) and for 2D imaging. Mappings for other special cases and for 3D imaging can be obtained similarly [19, 22].

5.5.1
Mapping for Steer Plane Wave Imaging

As mentioned before, images can be reconstructed with steered plane waves using Equation 5.31 or Equation 5.28. To steer a plane wave, linear time delays are applied to transducer elements:

$$\tau(x_1) = \frac{-x_1 \sin \zeta_T}{c} \tag{5.41}$$

where $x_1 \in (-D/2, D/2)$ is the position of the center of the element of an array transducer, D is the size of the transducer aperture, and ζ_T is the steering angle that is fixed for each transmission. To make the system causal, an additional constant delay may be added to the delay function (Equation 5.41) in practical implementations [19, 22].

Assuming $k_{x_T} = k \sin \zeta_T$, from Equation 5.28 or the 2D case of Equation 5.31, one obtains an inverse function for given values at (k'_x, k'_z):

$$\begin{cases} k_x = k'_x - k \sin \zeta_T \\ k \;\; = \dfrac{k'^2_z + k'^2_x}{2k'_z \cos \zeta_T + 2k'_x \sin \zeta_T} \end{cases} \tag{5.42}$$

To exclude evanescent waves, the condition for steered plane waves is $|k_x| \le k$ (notice that $k \ge 0$ and $|\zeta_T| < \pi/2$). With this condition, one set of boundaries in (k'_x, k'_z) can be determined by setting $k_x = k$ and $k_x = -k$, respectively, in Equation 5.28:

$$\begin{cases} k'_z = \dfrac{\cos \zeta_T}{\sin \zeta_T + 1} k'_x, & \text{if } k_x = k \\ k'_z = \dfrac{\cos \zeta_T}{\sin \zeta_T - 1} k'_x, & \text{if } k_x = -k \end{cases} \tag{5.43}$$

If the imaging system is band limited, that is, $k_{\min} \le k \le k_{\max}$, another two boundaries can be added using Equation 5.28 and $k_{x_T} = k \sin \zeta_T$:

$$\begin{cases} (k'_x - k_{\min} \sin \zeta_T)^2 + (k'_z - k_{\min} \cos \zeta_T)^2 = k^2_{\min}, & \text{if } k_x = k_{\min} \\ (k'_x - k_{\max} \sin \zeta_T)^2 + (k'_z - k_{\max} \cos \zeta_T)^2 = k^2_{\max}, & \text{if } k_x = k_{\max} \end{cases} \tag{5.44}$$

Outside of the region determined by the boundaries, values at (k'_x, k'_z) are simply set to 0. The mapping can be done with bilinear interpolation or any non-uniform fast Fourier transform (NUFFT) approach [81]. To increase the interpolation accuracy for the bilinear interpolation, data in the echo Fourier domain can be densified by zero padding or other signal processing methods as long as the original data are not aliased [82].

5.5.2
Mapping for Limited-Diffraction-Beam Imaging

5.5.2.1 General Case

For limited-diffraction array beam imaging, an inverse function of Equation 5.28 can be derived for given values at (k'_x, k'_z) [19, 22]:

$$\begin{cases} k_x = k'_x - k_{x_T} \\ k \;= \dfrac{\sqrt{\left(k'^2_z + k^2_{x_T} - (k'_x - k_{x_T})^2\right)^2 + 4k'^2_z(k'_x - k_{x_T})^2}}{2k'_z} \end{cases} \tag{5.45}$$

To exclude evanescent waves, both $|k_x| \le k$ and $|k_{x_T}| \le k$ must be satisfied in Equation 5.28 (where $k \ge 0$). For limited-diffraction array beam weighting, k_{x_T} is a constant in each transmission. This means that the transmit aperture weighting function is the same for all frequency components, k, in each transmission. From these conditions, one set of boundaries in (k'_x, k'_z) can be found by setting $k_x = k$ or $k_x = -k$ in Equation 5.28:

$$(k'_x - k_{x_T})^2 - k'^2_z = k^2_{x_T}, \text{ if } k_x = k \text{ or } k_x = -k \tag{5.46}$$

which is a hyperbolic function with its center shifted to $(k_{x_T}, 0)$. The hyperbolic function has two branches that intersect with the k'_x axis at two points, that is, at $k'_x = 0$ and $k'_x = 2k_{x_T}$, respectively. Another boundary can be found by setting $k_{x_T} = k$ or $k_{x_T} = -k$ in Equation 5.28, which gives a half circle centered at $(k_{x_T}, 0)$ with a radius of $|k_{x_T}|$ that intercepts with the hyperbolic curves at $(0, 0)$ and $(0, 2k_{x_T})$, respectively:

$$(k'_x - k_{x_T})^2 + k'^2_z = k^2_{x_T}, \text{ if } k_{x_T} = k \text{ or } k_{x_T} = -k \tag{5.47}$$

If the imaging system is band limited, that is, $k_{\min} \le k \le k_{\max}$, from Equation 5.28 another two circular boundaries can be obtained:

$$(k'_x - k_{x_T})^2 + (k'_z - \sqrt{k^2_{\min} - k^2_{x_T}})^2 = k^2_{\min}, \text{ if } k = k_{\min} \ge k_{x_T} \tag{5.48}$$

and

$$(k'_x - k_{x_T})^2 + (k'_z - \sqrt{k^2_{\max} - k^2_{x_T}})^2 = k^2_{\max}, \text{ if } k = k_{\max} \ge k_{x_T} \tag{5.49}$$

which further limit the size of the mapping area in (k'_x, k'_z). As k_{x_T} increases, low frequency components cannot be transmitted to illuminate objects, which could lower the energy efficiency. Outside of the region determined by the boundaries, values at (k'_x, k'_z) are simply set to 0. Similar to the steered plane wave case above, the mapping can be done with bilinear interpolation or any NUFFT approach [81]. To increase the interpolation accuracy for the bilinear interpolation, data in the echo Fourier domain can be densified with the zero padding or other signal processing methods as long as the original data are not aliased [82].

For limited-diffraction array beam transmissions, both sine and cosine aperture weightings are applied and thus the echoes need to be combined using Equation 5.35 to get two new sets of echoes before the mapping process above. The combination could be done in either echo or echo Fourier domain. Images can be reconstructed from the mapped data (see the paragraph below Equation 5.34).

5.5.2.2 **Special Case**

For a single plane wave imaging to achieve a high image frame rate, that is, letting $k_{x_T} = 0$, from Equation 5.45 we have Equation 40 of [16]:

$$\begin{cases} k_x = k'_x \\ k \ = \dfrac{k'^2_z + k'^2_x}{2k'_z} \end{cases} \tag{5.50}$$

Notice that Equation 5.50 can also be obtained from Equation 5.42 by letting $k_{x_T} = 0$. To exclude evanescent waves, $|k_x| \leq k$ must be satisfied in Equation 5.50.

5.6
High-Frame-Rate Imaging Techniques–Their Improvements and Applications

5.6.1
Aperture Weighting with Square Functions to Simplify Imaging System

5.6.1.1 **Applied to Transmission**

Traditional imaging methods such as D&S [63, 64] require a phase delay for each element of an array transducer to focus or steer a transmit beam. The phase delay makes it difficult to share transmitters among transducer elements. As a result, a large number of transmitters are needed, especially for an array transducer that has many elements such as a 2D array. Although limited-diffraction array beam imaging methods in Equation 5.32 and Equation 5.34 (or Equation 5.35) [22, 23] may reduce the number of transmitters, it would still need a large number of transmitters to realize the exact sine and cosine aperture weightings [19–23].

The need of a large number of transmitters may cause problems. For example, modern transmitters are linear high-voltage radio-frequency (RF) power amplifiers [30] to accommodate the need of applications such as nonlinear imaging [83] and coded excitations [84]. To maintain a good linearity over a broad bandwidth at a high output voltage, the transmitters may consume large amounts of power and thus they must be physically large to dissipate heat and avoid short circuiting. In addition, to produce exact sine and cosine weightings with an array transducer, each transducer element may need a complicated switching network to connect among a large number of transmitters from one transmission to another.

To reduce the number of transmitters, a method for limited-diffraction array beam imaging with square-function aperture weightings was developed in which the sine and cosine aperture weighting functions in Equation 5.32 and Equation 5.34 (or Equation 5.35) are approximated, respectively, with the following square-functions (where x is an argument of the sine or cosine function and should be replaced with corresponding variables in Equations 5.32 and 5.35) [19, 21]:

$$w_s(x) = \begin{cases} 1, & \sin(x) \geq 0 \\ -1, & \sin(x) < 0 \end{cases} \tag{5.51}$$

and

$$w_c(x) = \begin{cases} 1, & \cos(x) \geq 0 \\ -1, & \cos(x) < 0 \end{cases} \tag{5.52}$$

If k_{x_T}, k_{y_T}, or both k_{x_T} and k_{y_T} in Equation 5.32 and Equation 5.34 (or Equation 5.35) are zero, the corresponding sine functions are set to zero, that is, these beams are not transmitted. With the square-function approximations, a 3D imaging system may be developed with only two transmitters [19, 21]: one has an output voltage of a fixed amplitude, and the other has an inverted output from the first. Each transducer element is then connected to either one of the transmitters through an electronic switch that is controlled by a digital logic, depending on the sign of the sine and cosine functions at the position of the element. Combined with the high computation efficiency of the FFT algorithm used in the HFR imaging method [16–18], simplified HFR and high-quality 3D imaging systems can be reconstructed.

The square-function aperture weightings can also be implemented with a single transmitter to further reduce the number of transmitters (removing the inverting transmitter and setting the negative weighting amplitude to zero). In this case, transducer elements are switched on or off to the single transmitter before each transmission, which may simplify the switching circuits. However, the direct current (DC) offset in the weighting functions needs to be compensated during the image reconstruction. This may require additional transmissions with a DC weighting that may reduce the image frame rate and complicate the signal processing although the additional transmissions may be used to enhance the signal-to-noise ratio (SNR) for the center strip of the image. In addition, because about half of the transducer elements are not activated in each transmission (except for $k_{x_T} = k_{y_T} = 0$), the SNR of echo signals may be reduced (except for the DC weighting mentioned above).

5.6.1.2 Applied to Reception

It is worth noting that, because of the reciprocal relationship in Equation 5.22, where $\Phi^{R}_{\text{array}}(\mathbf{r}_0, t)$ and $\Phi^{T}_{\text{array}}(\mathbf{r}_0, t)$ are exchangeable, the square-function aperture weightings can also be applied to the reception beam forming to approximate the limited-diffraction array beam aperture weightings of echo signals [16–18, 20, 21, 76, 77]. This may simplify the hardware needed to produce $R_{k_x+k_{x_T}, k_y+k_{y_T}, k_z+k_{z_T}}(t)$ in Equation 5.22 for all k_x and k_y, given a pair of k_{x_T} and k_{y_T} in the transmission [20, 21]. In particular, with the square-function weighting in reception, simple analog summation and subtraction amplifiers could be used to produce all the required spatial frequency components at k_x and k_y in real-time to replace some of high-speed FFT [80] circuits [20, 21].

5.6.2
Diverging Beams with a Planar Array Transducer to Increase Image Frame Rate

To increase the field of view while maintaining a high image frame rate, a diverging beam can be used in transmission [25]. This method still uses Equation 5.31 and Equation 5.42 to reconstruct images approximately although, in theory, steered plane waves in transmissions should be used. Results show that with a few degrees of diverging angles, the effects on the quality of reconstructed images are not significant while image areas covered are increased [25].

5.6.3
Diverging Beams with a Curved Array Transducer to Increase Image Field of View

Another way to increase the field of view while maintaining a high image frame rate is to use a curved array transducer [24]. The advantage of using a curved array is that no time delays are necessary to produce a diverging beam and thus the number of transmitters needed may be reduced. However, with curved array transducers, the FFT [80, 85], in theory, may be difficult to use in image reconstructions, and thus the amount of computation may be increased.

5.6.4
Other Studies on Increasing Image Field of View

Methods have also been developed to increase the field of view of the HFR imaging method [16–18] in 2000 [76]. These methods use various techniques such as steered plane waves and limited-diffraction beams to increase the image field of view (also see claims 8 and 9 for steered plane waves and claim 3 for limited-diffraction beams in [18]) and were further studied in [19–22].

5.6.5
Coherent and Incoherent Superposition to Enhance Images and Increase Image Field of View

Due to a finite size of practical array transducers and the limitation of window sizes of the human body for ultrasonic imaging, each image reconstructed with ζ_T or k_{1_T} ($k_{1_T} = k_{x_T}$ in the 2D case) in Equation 5.42 or Equation 5.45 has a limited spatial extension [19–22] and thus the image field of view is limited. To increase the image field of view, multiple images reconstructed with various ζ_T or k_{1_T} or need to be combined. There are two ways to combine images. One is the coherent superposition that increases image resolution, reduces noise, and enhances image contrast. The other is incoherent superposition, which reduces image speckle noise rather than increasing image resolution [77].

5.6.6
Nonlinear Image Processing for Speckle Reduction

In addition to the incoherent image superposition mentioned above, various nonlinear image processing methods have been used to reduce speckles of the HFR images [77]. The methods used include frequency compounding, Axicon angle compounding, and the steering angle compounding.

5.6.7
Coordinate Rotation for Reduction of Computation

As ζ_T in Equation 5.42 or k_{1_T} in Equation 5.45 increases, the high-frequency components in the spatial echo Fourier domain also increase. This needs more points in the spatial Fourier domain to reconstruct an image, increasing the amount of computation. To reduce the computation, coordinates of transmission beams are rotated first to make $\zeta_T = 0$ or $k_{1_T} = 0$ in the echo Fourier domain to reconstruct images. Then, the reconstructed images are rotated back accordingly to recover the original orientations of the images before the superposition to form an image of a large field of view [26].

5.6.8
Reducing Number of Elements of Array Transducer

As mentioned previously, a 2D array transducer normally has tens of thousands of elements [65]. In addition, each transducer element needs an electronic circuit to handle the signals. Therefore, it is expensive to make such an array and its associated electronics and thus it is desirable to reduce the number of transducer elements whenever possible. A study [27] has been conducted for the trade-off between the number of elements of an array transducer and the quality of the HFR images [16–18]. Results show that it is possible to reduce the number of elements while maintaining a reasonable image quality [27].

5.6.9
A Study of Trade-Off between Image Quality and Data Densification

As mentioned previously, a nonlinear mapping between the echo Fourier domain and the object Fourier domain is necessary in order to use the FFT to reduce computations in image reconstructions. To increase the accuracy of the mapping, data in the echo Fourier domain may need to be densified before interpolation techniques such as the bilinear interpolation are used. However, there is a trade-off between image quality and an increase of the amount of computations due to the data densification. Therefore, a study on such a trade-off has been conducted for the HFR imaging [82]. Results show that reasonably good images can be reconstructed with only a small amount of densification of the echo data. If the non-uniform FFT method [81] is used for the mapping, a better trade-off could be possible at the expense of an increased complexity in interpolations.

5.6.10
Masking Method for Improving Image Quality

Because the image reconstruction theory in this paper is obtained under ideal assumptions, for example, $\mathbf{r}_1 = (x_1, y_1, 0)$ is continuous and its spatial extension is infinity, and practical array transducers for transmitting and receiving waves always have a finite size and have discrete coordinate values, images reconstructed contain not only plane wave components defined in Equation 5.22, but also include artifacts due to the imperfection of the practical imaging systems. Therefore, it is important to block the unwanted components of reconstructed images with spatial masks. The masks are usually designed to remove components that are in directions other than the designated transmission directions given by ζ_T or k_{1_T} ($k_{1_T} = k_{x_T}$ in the 2D case) in Equation 5.42 or Equation 5.45. Before the coherent superposition of images reconstructed with various ζ_T or k_{1_T}, proper masks are applied to each component image to improve image quality [87].

5.6.11
Reducing Clutter Noise by High-Pass Filtering

As the plane wave [19, 22] or waves that have small divergence angles [25] have a relatively flat wave front, in the HFR imaging, it is observed that there is clutter noise that appears in images as strips that are generally in parallel with the surface of the transducer. The clutter noise in the images is most obvious in anechoic areas, at deeper depths where receiver gain is high and echo signals are weak, and when the steering angle is small. The noise is caused by imperfect receiver electronics, multiple reflections among parallel objects, and multiple reflections between the objects and the transducer surface. To reduce the clutter noise and improve the quality of the HFR imaging method, a method using a spatial high-pass filtering of echo signals along axes that are in parallel with the surface of the transducer has been developed [88].

5.6.12
Obtaining Flow or Tissue Velocity Vectors for Functional Imaging

Because the imaging methods with steered plane waves or limited-diffraction array beams reconstruct complete images (as opposed to a line of image) with only one or a few transmissions, velocity vector images of moving objects such as the heart and the blood flow can be reconstructed with the HFR imaging methods [21, 23, 28]. This is different from the traditional Doppler method that only obtains the velocity vector component along the transmit beam and can be used for functional imaging for more accurate diagnoses of diseases [21, 28].

5.6.13
Strain and Strain Rate Imaging to Obtain Tissue Parameters or Organ Functions

The strain and strain rate imaging is important for accurate diagnoses of heart diseases. As mechanical properties of heart tissues change due to a lack of blood perfusion caused by blocked or partially blocked coronary arteries, the strain and strain rate of the heart may also change. The HFR imaging is especially useful for obtaining images of strain and strain rate of fast moving objects such as the heart [29, 66, 67] for medical diagnoses.

5.6.14
High-Frame-Rate Imaging Systems

To verify the HFR imaging theory developed above, a prototype HFR imaging system was developed [19, 21, 86]. This system has 128 independent linear high-voltage (up to ±144 V peak) and broadband RF (0.05–10 MHz) power amplifiers [30] for producing transmit beams and 128 independent high-gain and low-noise RF receivers. Images of a cycle of the beating heart of the author have been reconstructed with data acquired with this system and are displayed as a video clip [19].

In addition to the prototype HFR imaging system [19, 21, 86], a potential commercial HFR imaging system is proposed in Figure 5.1 [21].

5.7
Conclusion

As a continuation of the first volume of this book [1], this chapter has provided a detailed theoretical background of limited-diffraction beams [9–15, 62] such as Bessel beams [2, 3] and X waves [4–8], and applied the theory to develop the HFR imaging methods [16–23]. Various techniques for improving the HFR imaging methods and applications of the methods have been reviewed, including a prototype HFR imaging system [19, 21, 86] for verifying the developed HFR imaging methods experimentally and an illustration of a proposed commercial HFR imaging system (Figure 5.1 in [21]). The chapter can serve as a basis for future developments of novel imaging methods based on limited-diffraction beams.

References

1. Lu, J.-Y. (2008) in *Localized Waves, vol. 1, Chapter 4*, (eds H.E. Hernandez-Figueroa, M. Zamboni-Rached, and E. Recami), John Wiley & Sons, Inc., Hoboken, NJ, pp. 97–128, ISBN: 978-0-470-10885-7.
2. Lu, J.-Y. and Greenleaf, J.F. (1990) Ultrasonic nondiffracting transducer for medical imaging. *IEEE Trans. Ultrason. Ferroelectr. Freq. Control*, **37** (5), 438–447.
3. Lu, J.-Y. and Greenleaf, J. F. (1992) Ultrasonic nondiffracting transducer. US Patent 5081995, Issued Jan. 21, 1992.

4. Lu, J.-Y. and Greenleaf, J.F. (1991) Theory and acoustic experiments of nondiffracting X waves. 1991 IEEE Ultrasonics Symposium Proceedings, 91CH3079-1, Vol. 2, pp. 1155–1159, ISSN: 1051–0117.
5. Lu, J.-Y. and Greenleaf, J.F. (1992) Nondiffracting X waves–exact solutions to free-space scalar wave equation and their finite aperture realizations. *IEEE Trans. Ultrason. Ferroelectr. Freq. Control*, **39** (1), 19–31.
6. Lu, J.-Y. and Greenleaf, J.F. (1992) Experimental verification of nondiffracting X waves. *IEEE Trans. Ultrason. Ferroelectr. Freq. Control*, **39** (3), 441–446.
7. Lu, J.-Y. and Liu, A. (2000) An X wave transform. *IEEE Trans. Ultrason. Ferroelectr. Freq. Control*, **47** (6), 1472–1481.
8. Day, C. (2004) Intense X-shaped pulses of light propagate without spreading in water and other dispersive media, "Search and Discovery" column of *Phys. Today*, **57** (10), 25–26.
9. Lu, J.-Y., Zou, H., and Greenleaf, J.F. (1995) A new approach to obtain limited diffraction beams. *IEEE Trans. Ultrason. Ferroelectr. Freq. Control*, **42** (5), 850–853.
10. Lu, J.-Y. (1997) Designing limited diffraction beams. *IEEE Trans. Ultrason. Ferroelectr. Freq. Control*, **44** (1), 181–193.
11. Lu, J.-Y. (1995) Construction of limited diffraction beams with Bessel bases. 1995 IEEE Ultrasonics Symposium Proceedings, 95CH35844, Vol. 2, pp. 1393–1397, ISSN: 1051–0117.
12. Lu, J.-Y. (1997) Limited diffraction array beams. *Int. J. Imaging Syst. Technol.*, **8** (1), 126–136ISSN: 0899–9457.
13. Lu, J.-Y. (1995) Bowtie limited diffraction beams for low-sidelobe and large depth of field imaging. *IEEE Trans. Ultrason. Ferroelectr. Freq. Control*, **42** (6), 1050–1063.
14. Lu, J.-Y. (1996) Producing Bowtie limited diffraction beams with synthetic array experiment. *IEEE Trans. Ultrason. Ferroelectr. Freq. Control*, **43** (5), 893–900.
15. Lu, J.-Y. (1996) Method for reducing sidelobes of limited diffraction pulse-echo images. US Patent 5492121, Issued Feb. 20, 1996.
16. Lu, J.-Y. (1997) 2D and 3D high frame rate imaging with limited diffraction beams. *IEEE Trans. Ultrason. Ferroelectr. Freq. Control*, **44** (4), 839–856.
17. Lu, J.-Y. (1998) Experimental study of high frame rate imaging with limited diffraction beams. *IEEE Trans. Ultrason. Ferroelectr. Freq. Control*, **45** (1), 84–97.
18. Lu, J.-Y. and Greenleaf, J.F. (1998) High frame rate imaging with limited diffraction beams. US Patent 5720708, issued Feb. 24, 1998.
19. Lu, J.-Y., Cheng, J., and Wang, J. (2006) High frame rate imaging system for limited diffraction array beam imaging with square-wave aperture weightings. *IEEE Trans. Ultrason. Ferroelectr. Freq. Control*, **53** (10), 1796–1812.
20. Lu, J.-Y. and Wang, J. (2006) Square-wave aperture weightings for reception beam forming in high frame rate imaging. 2006 IEEE Ultrasonics Symposium Proceedings, 06CH37777, Vol. 1, pp. 124–127, ISSN: 1051–0117.
21. Lu, J.-Y. (2013) High frame rate imaging system. US Patent 8496585, issued July 30, 2013.
22. Cheng, J. and Lu, J.-Y. (2006) Extended high frame rate imaging method with limited diffraction beams. *IEEE Trans. Ultrason. Ferroelectr. Freq. Control*, **53** (5), 880–899.
23. Lu, J.-Y. and Cheng, J. (2011) System for extended high frame rate imaging with limited diffraction beams. US Patent 7957609, issued Jun. 7, 2011.
24. Peng, H. and Lu, J.-Y. (2002) High frame rate 2D and 3D imaging with a curved or cylindrical array. 2002 IEEE Ultrasonics Symposium Proceedings, 02CH37388, Vol. 2, pp. 1725–1728, ISSN: 1051–0117.
25. Lu, J.-Y. and Chen, H. (2011) High frame rate imaging with diverging beam transmission and Fourier reconstruction. 2011 IEEE Int. Ultrason. Symp. Proc., pp. 2221–2224, doi: 10.1109/ULTSYM.2011.0551.
26. Lu, J.-Y. and Kwon, S.-J. (2007) Simplification of high frame rate imaging system with coordinate rotation. 2007 IEEE Ultrasonics Symposium Proceedings, 07CH37920, Vol. 1, pp. 33–36, ISSN: 1051–0117.

27. Lu, J.-Y. and He, S. (1999) High frame rate imaging with a small number of array elements. *IEEE Trans. Ultrason. Ferroelectr. Freq. Control*, **46** (6), 1416–1421.
28. Lu, J.-Y., Wang, Z., and Kwon, S.-J. (2006) Blood flow velocity vector imaging with high frame rate imaging methods. 2006 IEEE Ultrasonics Symposium Proceedings, 06CH37777, Vol. 2, pp. 963–966, ISSN: 1051–0117.
29. Chen, H. and Lu, J.-Y. (2012) Estimation of two-dimensional strain rate based on high frame rate ultrasound imaging method. Proceedings of Meetings on Acoustics (POMA), Acoustical Society of America, January 13, Vol. 14, pp. 1–12, Article 020001, doi: 10.1121/1.3681323
30. Lu, J.-Y. and Waugaman, J.L. (2004) Development of a linear power amplifier for high frame rate imaging system. 2004 IEEE Ultrasonics Symposium Proceedings, 04CH37553C, Vol. 2, pp. 1413–1416, ISSN: 1051–0117.
31. Lu, J.-Y. and Cheng, J. (2005) Field computation for two-dimensional array transducers with limited diffraction array beams. *Ultrason. Imaging*, **27** (4), 237–255.
32. Lu, J.-Y. and Greenleaf, J.F. (1990) Evaluation of a nondiffracting transducer for tissue characterization. 1990 IEEE Ultrasonics Symposium Proceedings, 90CH2938-9, Vol. 2, pp. 795–798, ISSN: 1051–0117.
33. Lu, J.-Y. and Greenleaf, J.F. (1991) Pulse-echo imaging using a nondiffracting beam transducer. *Ultrasound Med. Biol.*, **17** (3), 265–281.
34. Lu, J.-Y., Song, T.K., Kinnick, R.R., and Greenleaf, J.F. (1993) In vitro and in vivo real-time imaging with ultrasonic limited diffraction beams. *IEEE Trans. Med. Imaging*, **12** (4), 819–829.
35. Lu, J.-Y., Fatemi, M., and Greenleaf, J.F. (1996) Pulse-echo imaging with X wave. in *Acoustic Imaging*, Vol. 22 (ed. P. Tortoli), Plenum Press, New York, pp. 191–196, ISBN: 0-306-45364-9.
36. Lu, J.-Y., Xu, X.-L., Zou, H., and Greenleaf, J.F. (1995) Application of Bessel beam for Doppler velocity estimation. *IEEE Trans. Ultrason. Ferroelectr. Freq. Control*, **42** (4), 649–662.
37. Lu, J.-Y. (1996) Improving accuracy of transverse velocity measurement with a new limited diffraction beam. 1996 IEEE Ultrasonics Symposium Proceedings, 96CH35993, Vol. 2, pp. 1255–1260, ISSN: 1051–0117.
38. Lu, J.-Y. and Greenleaf, J.F. (1993) Producing deep depth of field and depth-independent resolution in NDE with limited diffraction beams. *Ultrason. Imaging*, **15** (2), 134–149.
39. Lu, J.-Y., Cheng, J., and Cameron, B. (2002) Low sidelobe limited diffraction optical coherence tomography. *Proc. of SPIE*, **4619**, pp. 300–311, ISBN: 0-8194-4358-1.
40. Lu, J.-Y. (1997) High-speed transmissions of images with limited diffraction beams. in *Acoustic Imaging*, Vol. 23 (eds S. Lees and L.A. Ferrari), Kluwer Acadmic/Plenum Press, New York, pp. 249–254, ISBN: 0-306-45768-7.
41. Lu, J.-Y. and He, S. (1999) Optical X wave communications. *Opt. Commun.*, **161**, 187–192.
42. Lu, J.-Y. (1997) Transmit-receive dynamic focusing with limited diffraction beams. 1997 IEEE Ultrasonics Symposium Proceedings, 97CH36118, Vol. 2, pp. 1543–1546, ISSN: 1051–0117.
43. Lu, J.-Y., Zou, H., and Greenleaf, J.F. (1994) Biomedical ultrasound beam forming. *Ultrasound Med. Biol.*, **20** (5), 403–428.
44. Lu, J.-Y. and Greenleaf, J.F. (1992) Diffraction-limited beams and their applications for ultrasonic imaging and tissue characterization. *Proc. of SPIE*, **1733**, pp. 92–119, ISBN: 0-8194-0906-5.
45. J.-Y. Lu (1999) Principle and applications of limited diffraction beams, *Acta Phys. Sin.*, **8** (Suppl.), 22–26, .
46. Stratton, J.A. (1941) *Electromagnetic Theory*, McGraw-Hill, New York and London, p. 356.
47. Durnin, J. (1987) Exact solutions for nondiffracting beams. I. The scalar theory, *J. Opt. Soc. Am. A*, **4** (4), 651–654.
48. Hsu, D.K., Margetan, F.J., and Thompson, D.O. (1989) Bessel beam ultrasonic transducer: fabrication method and experimental results. *Appl. Phys. Lett.*, **55** (20), 2066–2068.

49. Campbell, J.A. and Soloway, S. (1990) Generation of a nondiffracting beam with frequency independent beam width. *J. Acoust. Soc. Am.*, **88** (5), 2467–2477.
50. Saari, P. and Reivelt, K. (1997) Evidence of X-shaped propagation-invariant localized light waves. *Phys. Rev. Lett.*, **79**, 4135–4138.
51. Besieris, I., Abdel-Rahman, M., Shaarawi, A., and Chatzipetros, A. (1998) Two fundamental representations of localized pulse solutions to the scalar wave equation. *Prog. Electromagn. Res. (PIER)*, **19**, 1–48.
52. Saari, P. and Reivelt, K. (2004) Generation and classification of localized waves by Lorentz transformations in Fourier space. *Phys. Rev. E*, **69**, 036612.
53. Zamboni-Rached, M., Nóbrega, K.Z., Recami, E., and Hernández-Figueroa, H.E. (2002) Superluminal X-shaped beams propagating without distortion along a coaxial guide. *Phys. Rev. E*, **66**, 046617.
54. Zamboni-Rached, M., Fontana, F., and Recami, E. (2003) Superluminal localized solutions to Maxwell equations propagating along a waveguide: the finite-energy case. *Phys. Rev. E*, **67**, 036620.
55. Zamboni-Rached, M., Recami, E., and Fontana, F. (2001) Superluminal localized solutions to Maxwell equations propagating along a normal-sized waveguide. *Phys. Rev. E*, **64**, 066603.
56. Salo, J., Friberg, A.T., and Salomaa, M.M. (2001) Orthogonal X waves. *J. Phys. A: Math. Gen.*, **34**, 9319–9327.
57. Recami, E., Zamboni-Rached, M., and Dartora, C.A. (2004) Localized X-shaped field generated by a superluminal electric charge. *Phys. Rev. E*, **69**, 027602.
58. Zamboni-Rached, M., Recami, E., and Hernández-Figueroa, H.E. (2005) Theory of frozen waves: modeling the shape of stationary wave fields. *J. Opt. Soc. Am. A*, **22** (11), 2465–2475.
59. Brittingham, J.N. (1983) Focus wave modes in homogeneous Maxwell's equations: transverse electric mode. *J. Appl. Phys.*, **54** (3), 1179–1189.
60. Ziolkowski, R.W. (1985) Exact solutions of the wave equation with complex source locations. *J. Math. Phys.*, **26** (4), 861–863.
61. Ziolkowski, R.W., Lewis, D.K., and Cook, B.D. (1989) Evidence of localized wave transmission. *Phys. Rev. Lett.*, **62** (2), 147–150.
62. Lu, J.-Y. and Greenleaf, J.F. (1993) Sidelobe reduction for limited diffraction pulse-echo systems. *IEEE Trans. Ultrason. Ferroelectr. Freq. Control*, **40** (6), 735–746.
63. Ozaki, Y., Sumitani, H., Tomoda, T., and Tanaka, M. (1988) A new system for real-time synthetic aperture ultrasonic imaging. *IEEE Trans. Ultrason. Ferroelectr. Freq. Control*, **35** (6), 828–838.
64. Steinberg, B.D. (1988) Microwave imaging of aircraft. *Proc. IEEE*, **76** (12), 1578–1592.
65. Lu, J.-Y. and Greenleaf, J.F. (1994) A study of two-dimensional array transducers for limited diffraction beams. *IEEE Trans. Ultrason. Ferroelectr. Freq. Control*, **41** (5), 724–739.
66. Montaldo, G., Tanter, M., Bercoff, J., Benech, N., and Fink, M. (2009) Coherent plane-wave compounding for very high frame rate ultrasonography and transient elastography. *IEEE Trans. Ultrason. Ferroelectr. Freq. Control*, **56** (3), 489–506.
67. Macé, E., Montaldo, G., Cohen, I., Baulac, M., Fink, M., and Tanter, M. (2011) Functional ultrasound imaging of the brain. *Nat. Methods*, **8** (8), 662–664.
68. Wade, G. (2000) Human uses of ultrasound: ancient and modern. *Ultrasonics*, **38**, 1–5.
69. Morse, P.M. and Feshbach, H. (1953) *Methods of Theoretical Physics, Part I*, McGraw-Hill, New York, p. 620.
70. Kino, G.S. (1987) *Acoustic Waves: Devices, Imaging and Analog Signal Processing*, Prentice-Hall, Englewood Cliffs, NJ.
71. Bracewell, R. (1965) *The Fourier Transform and its Applications* Chapter 4 and 6, McGraw-Hill, New York.
72. Kak, A.C. and Slaney, M. (1987) *Principle of Computerized Tomographic Imaging* Chapter 6, IEEE Press, New York.
73. Born, M. and Wolf, E. (1999) *Principles of Optics*, 7th edn Chapter 13, Cambridge University Press, Cambridge.

74. Sherman, G.C. (1967) Application of the convolution theorem to Rayleigh's integral formulas. *J. Opt. Soc. Am.*, **57**, 546–547.

75. Goodman, J.W. (1968) *Introduction to Fourier Optics* Chapter 2 to 4, McGraw-Hill, New York.

76. Lu, J.-Y. and He, S. (2000) Increasing field of view of high frame rate ultrasonic imaging. *J. Acoust. Soc. Am.*, **107** (5), 2779 (Abstract).

77. J.-Y. Lu, Nonlinear processing for high frame rate imaging, *J. Ultrasound Med.*, **18**, (3, Suppl.), S50, 1999 (Abstract).

78. Soumekh, M. (1992) Array imaging with beam-steered data. *IEEE Trans. Image Process*, **1** (3), 379–390.

79. Burckhardt, C.B., Hoffmann, H., and Grandchamp, P.A. (1973) Ultrasound Axicon: a device for focusing over a large depth. *J. Acoust. Soc. Am.*, **54**, 1628–1630.

80. Cooley, J.W. and Tukey, J.W. (1965) An algorithm for the machine calculation of complex Fourier series. *Math. Comput.*, **19**, 297–301.

81. Fessler, J. and Sutton, B. (2003) Nonuniform fast fourier transforms using min-max interpolation. *IEEE Trans. Signal Process.*, **51** (2), 560–574.

82. Lu, J.-Y. (2008) Effects of data density of echo Fourier domain on quality of high frame rate imaging. 2008 IEEE International Ultrasonics Symposium Proceedings, CFP08ULT, Vol. 1, pp. 974–977, ISSN: 1051–0117, doi: 10.1109/ULTSYM.2008.0235

83. Averkiou, M.A., Roundhill, D.R., and Powers, J.E. (1997) A new imaging technique based on the nonlinear properties of tissues. 1997 IEEE Ultrasonics Symposium Proceedings, 97CH36118, Vol. 2, pp. 1561–1566, ISSN: 1051–0117.

84. O'Donnell, M. (1992) Coded excitation system for improving the penetration of real-time phased-array imaging systems. *IEEE Trans. Ultrason. Ferroelectr. Freq. Control*, **39** (3), 341–351.

85. Oppenheim, A.V. and Schafer, R.W. (1975) *Digital Signal Processing*, Prentice Hall, Saddle River, NJ.

86. Lu, J.-Y. (2003) A multimedia example. *IEEE Trans. Ultrason. Ferroelectr. Freq. Control*, **50** (9), 1078.

87. Lu, J.-Y. (2012) Effects of Masks on Reconstruction of High-Frame-Rate Images, *2012 IEEE International Ultrasonics Symposium Proceedings, CFP12ULT*, pp. 2137–2140, (ISSN: 1948-5727) doi: 10.1109/ULTSYM.2012.0533.

88. Lu, J.-Y., Reducing clutter noise in fast ultrasound imaging with transverse high-pass filtering, *2013 IEEE International Ultrasonics Symposium Proceedings* (Joint UFFC, EFTF, and PFM Symposium) (to be published in 2013).